Title
Fabrication and Characterization of Epitaxial P-I-N Germanium X-ray Photodiodes

Author
Guo, Ziang

Publication Date
2023

Peer reviewed|Thesis/dissertation

Fabrication and Characterization of Epitaxial P-I-N Germanium X-ray Photodiodes

By

ZIANG GUO
THESIS

Submitted in partial satisfaction of the requirements for the degree of

MASTER OF SCIENCE

in

Electrical Engineering

in the

OFFICE OF GRADUATE STUDIES

of the

UNIVERSITY OF CALIFORNIA

DAVIS

Approved:

Charles E. Hunt

Saif Islam

Klaus Van Benthem

Committee in Charge

2023

Acknowledgement

This research was made possible by Arthur Carpenter from Lawrence Livermore National Lab (LLNL). Special thanks to Professor Diego R. Yankelevich for providing critical laser equipments, and to Sergey Mistyuk for helping with the completion of this thesis.

Abstract

A fabrication process for a p-i-n germanium photodiode design was developed for epitaxially-grown germanium wafers. Devices fabricated were tested for DC large-signal I-V characteristics and AC temporal responses. The germanium wafers were in-situ doped with the p-i-n structure to minimize dark current generated by lattice defects. With higher atomic mass, germanium provides stronger stopping power for high-energy photons in the hard X-ray regime above 20 keV. The fabrication process developed was able to achieve 86.7% yield with a 2-day lead time. The p-i-n devices fabricated were measured to have an average turn-on voltage of 1.6 V, an average dark current of 3.9 mA with ambient illumination. The average breakdown voltage was measured to be -11.85 V. At -40 V applied bias, the fabricated germanium diodes were able to generate a maximum signal level 229% of that generated by commercially available AXUV silicon-based detectors. The average 87% rise time of fabricated germanium devices was 150 nanoseconds and the average 13% fall time was 128 nanoseconds. The germanium devices achieved an average frametime of 278 ns. The signal-to-noise ratio measured was 20.9 with $\ll 10\%$ illuminated area at -40 V bias. In general, the fabrication process was successful in fabricating germanium p-i-n photodidoes with satisfactory temporal and DC characteristics. The devices were also able to demonstrate the superior performance expected from germanium-based devices.

Chapter 1

1.1 Background

High-energy photons have been a useful diagnosis and metrology tool in many fields of scientific research since the beginning of radiography. However, it is proven difficult to efficiently capture and image photons with energies in the 20 keV and above range (hard X-rays) due to poor stopping power of most materials. The most common ways of imaging hard X-ray photons usually involve a step of photon down-conversion where the high energy photons are first converted to lower energy photons through photocathode emission or scintillation before being imaged by either phosphorous screens or semiconductor sensors [1]. While widely used in the medical field for diagnosis, indirect imaging is not suitable for high-speed, high-precision imaging needs as the temporal and spatial resolutions are reduced by the down-conversion process.

The alternative to photon down-conversion is direct imaging where the signal is generated directly by absorbing the incoming high-energy photons. Commercial silicon-based hard X-ray detectors are available for purchase but does not provide the most ideal performance due to the requirement of ultra-thick ($\sim$500μm) absorption regions to achieve a desirable quantum efficiency [2]. This is due to the poor attenuation constant of silicon at X-ray energies [3]. The thick absorption region will significantly impact the temporal resolution of the detector.

With the significant draw backs of silicon-based direct imaging sensors and indirect imaging methods, improvements on the performance of hard X-ray sensor lie in the use of novel materials. There has been on-going researches on novel semiconducting materials with high absorption coefficients in the hard X-ray energy range. Materials such as cadmium telluride and gallium arsenide have outstanding linear attenuation coefficient at 80 keV. However, these materials are not suitable for imaging purposes due to low carrier mobilities and/or small bandgaps leading to high thermal noise[4][5].

1.2 Research Description

This research focuses on the fabrication of P-I-N germanium photodiodes designed for high-speed, high-efficiency imaging of hard X-ray photons. The photodiode devices were made using in-situ doped epitaxially-grown germanium wafers. Full wafer-to-device processes were developed for photolithographic patterning, material deposition, and packaging of the germanium dies.

Fabricated devices were tested on a probe station for both DC and transient response as characterization. The voltage-current behavior and the photoelectron excitation-relaxation waveform were measured with a 10-nanosecond, 532-nanometer green laser and analyzed to quantify device performance.

1.3 P-I-N Diode Operation

A semiconductor photodetector operates by measuring the flow (current) of the excess carriers generated by the incident light and collected by the metal contacts. When photons with energies higher than the bandgap of the semiconductor is absorbed, the energy of said photons will be used to generate electron-hole pairs (EHP) which will then formulate the conduction currents. It is thus imperial that the generation and recombination mechanisms of the germanium P-I-N diodes are correctly understood.

As shown in Figure 1, a P-I-N diode has two distinct regions. The regions can be divided into two parts: the intrinsic depletion region, and the doped quasi-neutral regions. Among the two, it is obvious that the dominant contributor to the total photocurrent will be the generation in the intrinsic region due to its substantial width. In the intrinsic region, assuming there is little lattice defects, most EHP generation will occur through direct band-to-band generation where an electron gains sufficient energy from the incident photons to be promoted from the valence band to the conduction band [6]. An energy band diagram of a P-I-N junction with the conduction mechanism is shown in Figure 2.

In the quasi-neutral regions, the presence of dopant impurities will also enable R-G

center generations where mid-gap donor/acceptor levels facilitate the generation process. We assume that there is no generation in the substrate of the devices as most X-ray photons should be absorbed in the device itself.

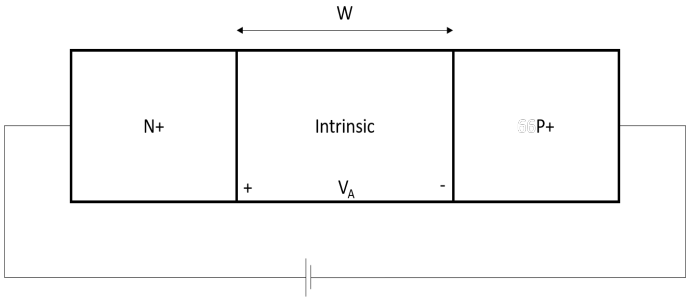

Figure 1. Typical structure of a P-I-N diode.

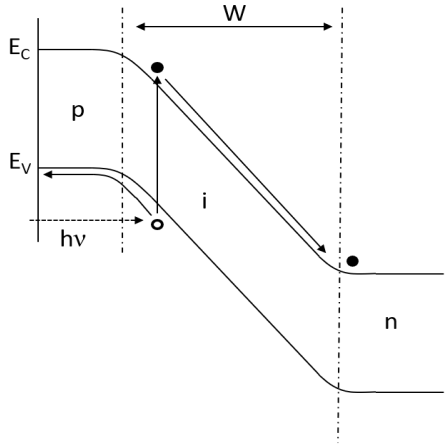

Figure 2. P-I-N diode energy band diagram and conduction mechanism.

1.3.1 Low Frequency Behavior

When a sufficient reverse bias is applied, the intrinsic region will be depleted of its low amount of intrinsic carriers and become part of the space-charge region under the influence of the electric field. Carriers generated inside the intrinsic region will then be accelerated by the electric field and drift towards the quasi-neutral regions and then collected by metal

anodes/cathodes. In reverse bias, the dominant component will be the EHPs generated in the intrinsic region. The current can be modeled as

$$I_r = -\frac{qAn_iW}{2\tau_0}$$

where τ_0 denotes the carrier generation lifetime in the depletion region [7]. The carrier generation lifetime is dependent on many variables with dopant concentration being the dominant one. Figure 3 shows a graph of τ_0 vs. doping concentration in both n- and p-type germanium.

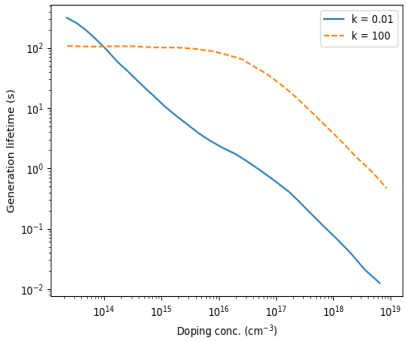

Figure 3. Carrier generation lifetime vs. doping concentration in n- and p-type germanium at high- and low-level injection ($k = \frac{N_{\text{injected}}}{N_{\text{doping}}}$). Data from [8].

1.3.2 High Frequency Behavior

At higher operating frequencies, the carrier transport time across the intrinsic region needs to be taken into consideration. For ultra-fast frame times, it is necessary to design devices with transport times in mind. Assuming a carrier drift velocity of v_{sl}, the transit time is

$$t_r = \frac{W}{v_{sl}}$$

The incident photon flux density at high frequencies cannot be assumed to be a constant

value. Instead, it should be expressed as

$$\Phi = \Phi_1 e^{j\omega t}$$

Then the resulting short-circuit diode current density under illumination is

$$J_{sc} = \frac{q\Phi_1(1 - e^{j\omega t_r})}{j\omega t_r} e^{j\omega t}$$

It is seen that for incident photon frequencies higher than ωt_r, the photocurrent generated in the diode drops substantially as the detection speed is limited by the carrier transit time [9].

1.4 Carrier R-G in Germanium

1.4.1 Generation

As discussed in Section 1.3, the dominant generation mechanism in germanium P-I-N photodiodes is the direct band-to-band generation. Since the devices mainly operate at room temperature or higher, thermionic emission also contributes to the diode current as noise when the excitation level is low.

1.4.2 Recombination

In order for any signal to be collected at the metal contacts, the carriers must not recombine during their travel in the germanium material. It it thus important for us to understand the contributing recombination mechanisms present in germanium.

Under normal circumstances, direct band-to-band recombination does not contribute significantly in germanium [10]. Instead, the majority of the recombination events are non-radiative trap recombinations at impurity sites or lattice defects (SRH recombination).[11] The rate at which SRH recombination occurs is dependent on the trap capture coefficient

and the trap density, both of which depends on the impurity concentrations. The lifetime of carriers vs. dopant concentration has been modeled and measured by multiple literature as shown in Figure 4(a) and Figure 4(b).

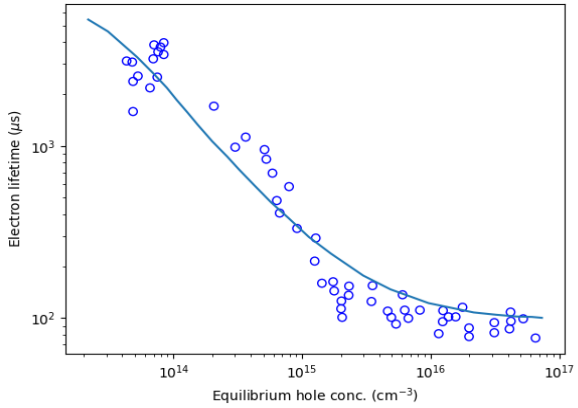

Figure 4(a). Dependence of the electrons lifetime vs. equilibrium hole concentration. Data from [12].

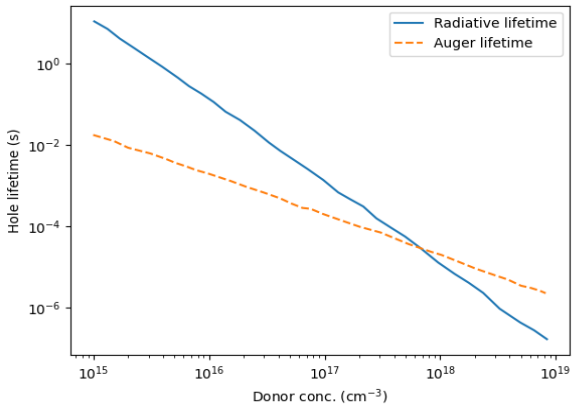

Figure 4(b). Dependence of the hole lifetime vs. equilibrium electron concentration. Data from [13].

The minority carrier lifetime dictates the decay of excess minority carrier concentration with the relation

$$\Delta = \Delta_0 e^{-\frac{t}{\tau}}$$

Chapter 2

2.1 Device Structure

The germanium P-I-N diodes are fabricated on epitaxially-grown in-situ doped germanium wafers provided by Lawrence Semiconductor Research Lab (LSRL). Doped and intrinsic germanium layers were grown on top of an intrinsic low-defect germanium wafer. The photodiodes were designed to be illuminated on the p-doped side. A 19-μm passivation layer is established on the p-side using PI-2610 polyimide. P-side metallic contact was formed using 200 nanometers of gold and 200 nanometers of palladium. An 1-nanometer alumina tunneling interface was deposited on the substrate side of the device to terminate surface states and reduce Fermi-level pinning [14]. A 70-nanometer nickel layer constitutes the metallic contact on the substrate side. A device cross-section can be seen in Figure 5.

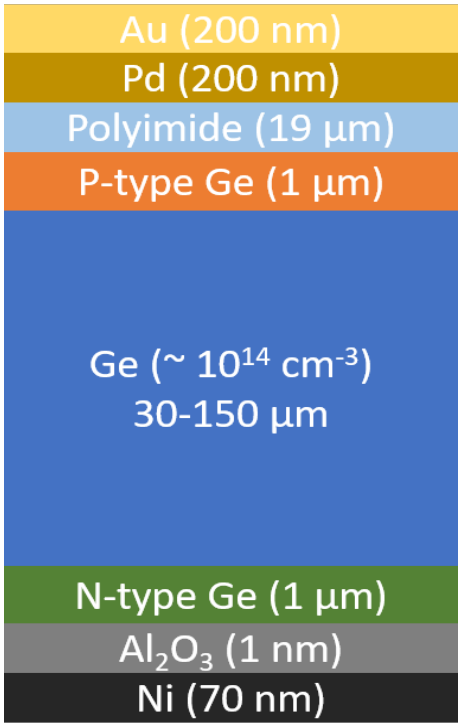

Figure 5. Device cross-section (not to scale)

2.2 Process Development

2.2.1 Wafer Cleaning

Before the bare wafer can be used for fabrication, rigorous cleaning must be done to remove any organics deposited from being exposed to open air and other possible surface contaminants from shipping and handling. The industry standard for cleaning silicon wafers is the RCA cleaning process. Composing of three steps that removes surface organics, the native oxide layer, and ionic contaminant, the RCA clean is a comprehensive cleaning routine [15]. However, RCA does not apply to our germanium wafers. The RCA process uses acidic etching solutions to remove the native oxide layer, oxidizes the exposed surface to separate ionic contaminants, and then remove the grown oxide layer for a pristine bare silicon surface. Since our wafer was in-situ doped inside the epitaxy reactor, RCA clean would strip away the top p-doped layer and affect device design. For the same reason, aggressive corrosives such as piranha cannot be used [16].

Our alternative to the RCA clean is the use of organic solvents to remove airborne contaminants. A sequence of acetone, methanol, and isopropyl alcohol are used to wash any particle and organic that was attracted from the ambient air. A sonicator is used to agitate the solvents to improve cleaning effectiveness. A DI-water rinse at the end removes any remaining solvents and residues from the surface.

2.2.2 Photoresist Processing

The pattern transfer for device fabrication is carried out using photolithography. To ensure the quality of the pattern transfer process, it is important that a consistent, defect-free photoresist film can be deposited on the germanium surface. The selected photoresist for the fabrication process was Futurrex NR78-8000P negative-tone i-line photoresist. The photoresist was chosen for its superior temperature resistance and the ability to from extra-thick coatings and function as resilient etch-stops. The thickness of the PR must be chosen so that

a balance is achieved between film stability and exposure resolution. A small amount of O_2 plasma is present during the RIE processes and can damage the PR layer. But a thick PR layer will cause more refraction inside the film and reduce the maximum resolution available. The selected thickness is 11 micrometers.

A spin-curve documenting the spin RPM vs. film thickness was provided by the manufacturer but only valid for silicon surfaces. Germanium surfaces have different characteristics and surface potential that affects thin-film adhesion of the photoresist. Multiple empirical tests were performed with slightly altered spin recipes and bake parameters had to be carried out to optimize the deposition of photoresist films. Combinations of spin speeds, adhesion promoters, and bake environments were tested. The film quality was qualitatively determined through a combination of visual inspection for pin-holes and film tears and film uniformity inspection under an optical microscope.

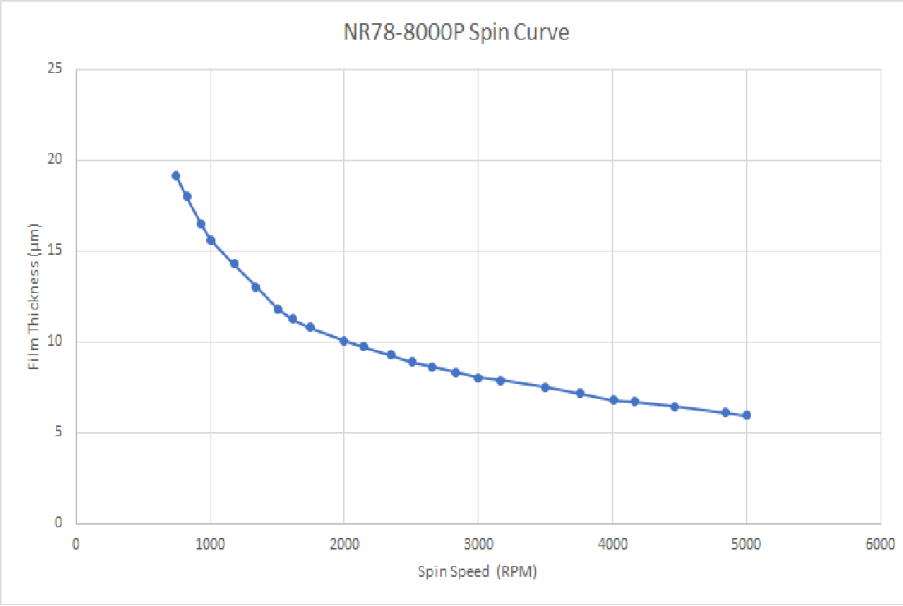

Figure 6. NR78-8000P spin curve as provided by manufacturer. Data from [17].

It was ultimately determined that a 40-second spin at 1750 RPM with 1-second spin-up and spin-down generates the most uniform photoresist film. Bake out was conducted on a hotplate at 120 °C with a pre-heated borosilicate glass panel as support for 7 minutes. The

longer bake time is to facilitate the lower thermal conductivity of germanium compared to silicon. The pre-heated glass plane allows for even heat transfer and dramatically reduces the amount of pin-holes generated. As seen in Figure 7(a) and 7(b), the use of a glass plane greatly reduces the density of resulting pin-holes.

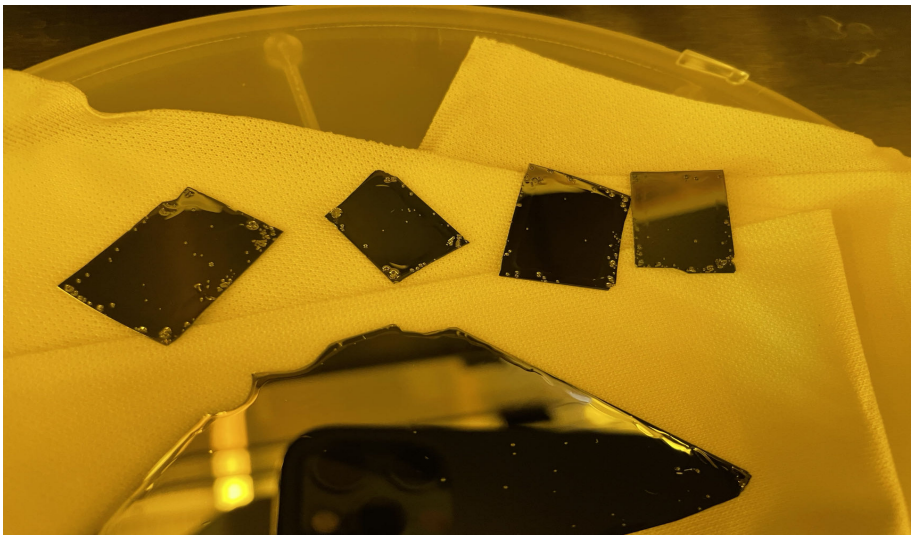

Figure 7(a). Photoresist film baked out without glass panel. Pin-holes are clearly visible around chip edges.

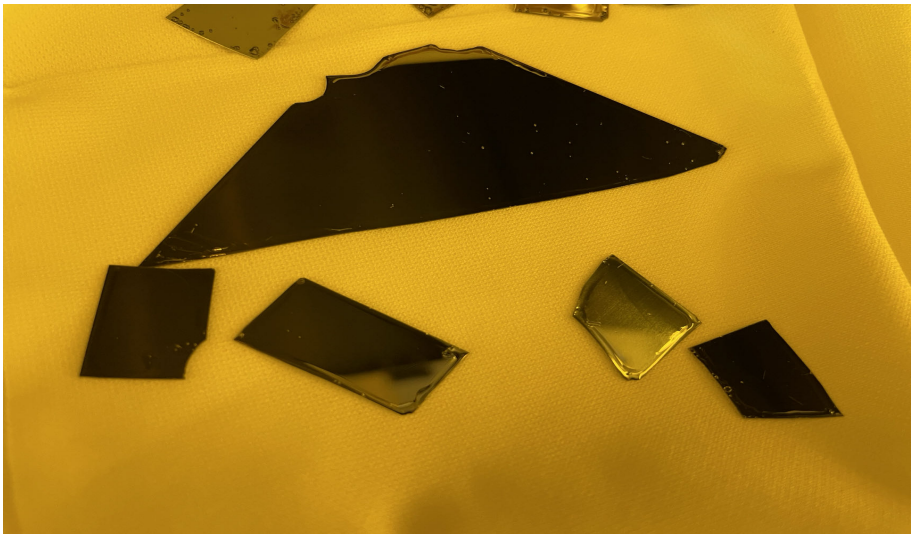

Figure 7(b). Photoresist film baked out with glass panel. Pin-hole density is greatly reduced.

For resist stripping, a wet chemical process was used instead of plasma ashing to ensure the complete removal of residues and minimize potential surface damage caused by ion bombardment. The photoresist stripper selected was the RR-41 designed to be used with Futurrex photoresists. A 5-minute bath in 85 °C RR-41 followed by a standard three-step solvent cleaning will remove hardened photoresists. RR-41 is also used in the liftoff process after p-side metalization. Liftoff is easier to implement than etch back as there is no involvement of aggressive etching chemicals.

2.2.3 Exposure

The deposited photoresist layer was exposed using a GCA 8500 i-line projection stepper. The stepper exposes the photoresist using a 365-nm mercury vapor lamp with a uniform illumination strength of $\approx$270 mW/cm^{-2}. Considering that the devices being made are much larger than the resolution limit of both the photoresist and the stepper, and to eliminate the effects of lamp power degradation, the exposure timer is set to always over-expose the sample. The exposure dosage and the focus offset depth were determined after performing an exposure calibration where a matrix of squares exposed with different dosage and focus depth was generated and developed. The matrix was examined under an optical microscope to determine the best combination of dosage and focus. Figure 8(a) and 8(b) offer a good comparison between a good dosage/focus and a bad combination.

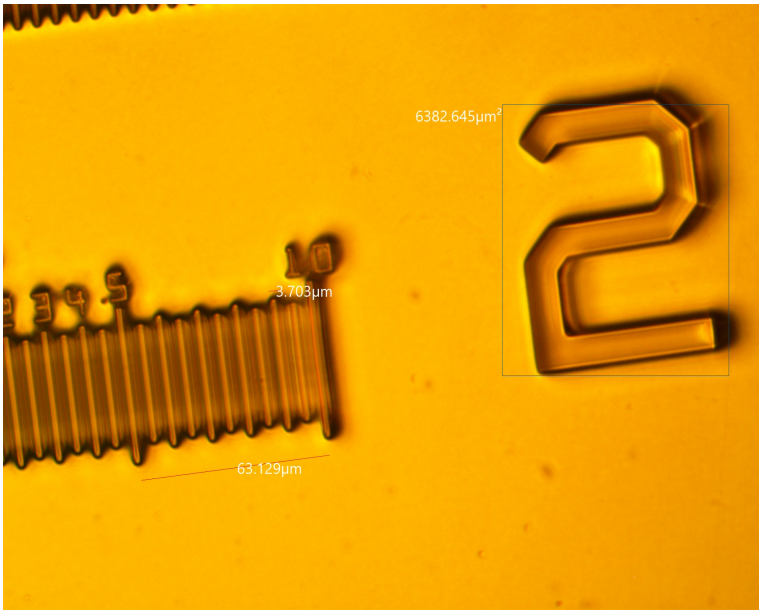

Figure 8(a). Good exposure dosage and focus depth

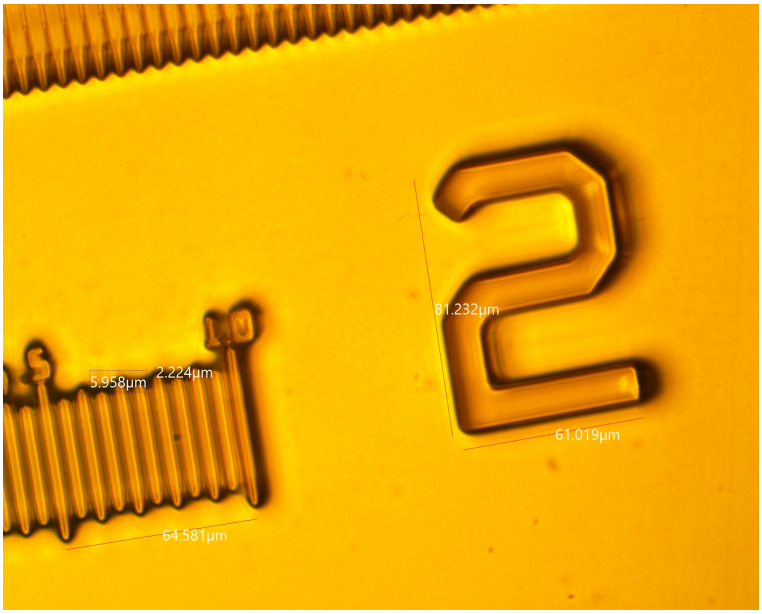

Figure 8(b). Less than desirable exposure dosage and focus (reduced feature details and blurry edges)

2.2.4 Reactive Ion Etching

To maximize our control over the etching profile and reduce the chance of introducing chemical contaminants, reactive ion etching (RIE) was selected as the primary patterning tool over traditional wet chemical etching. The RIE process utilizes a combination of O_2 and CF_4 to etch the germanium surface. The plasma power was 150 W with 40 sccm CF_4 and 5 sccm O_2. The etching duration is 5 minutes for etching of isolation trenches. The PlasmaTherm Vision 320 RIE is capable of automatically maintaining the chamber atmosphere according to the preset recipe.

The same RIE machine was used to etch and pattern the PI-2610 polyimide layer to create openings for metal contacts. Oxygen plasma was used to etch away PI-2610. The plasma power used was 204 W with 7 sccm O_2. Since oxygen plasma alone does not etch the germanium surface significantly [18], the etching duration is 15 minutes to ensure complete removal of PI-2610 at desired locations.

2.2.5 Cleaning and Passivation

Before the metalization, the p-side of the device must be cleaned and passivated. A cleaning step removes surface native oxides deposited when the sample was exposed to the atmosphere. Unlike silicon, germanium is unable to form a dense, consistent native oxide layer. Any remaining GeO_x layer will introduce surface states that promotes dark current in the finished devices. The surface must then be passivated to prevent future oxide growth.

Oxide stripping was performed in 7.2% HCl (1:4 36% HCl and DI water) [19]. The germanium samples were submerged in the solution for 1 minute before rinse off with water. Immediately after the strip, the samples were spin-coated with PI-2610 polyimide and cured in an oven using recipes provided by the manufacturer. The film quality was verified by visual inspection of the sample surface. As seen in Figure 9, there is no visible color gradient caused by non-uniformity, nor is there pin-holes or film tears.

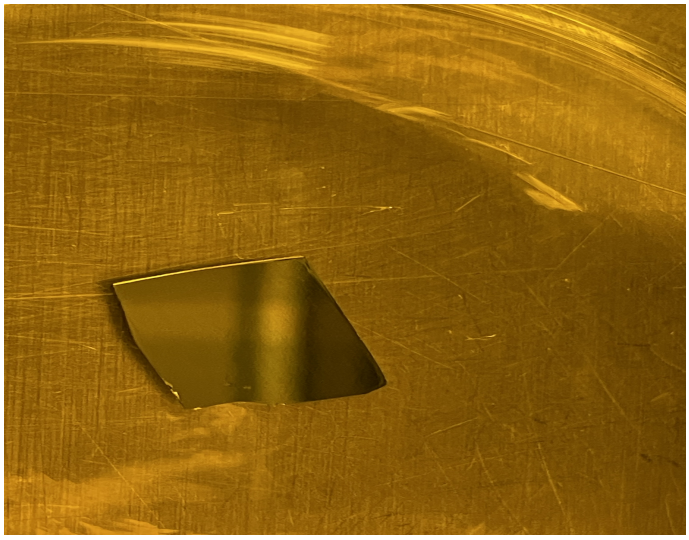

Figure 9. Sample after PI-2610 spin-on. Surface uniformity is satisfactory with minimal defects.

2.2.6 Metalization

The metalization process of our germanium photodiode must be split into two distinct process steps due to the vertical nature of the design. The exact metalization recipe must also be tailor-made to the properties of germanium itself to maximize contact performance and ensure metal adhesion.

- For the p-side contact, a metal stack consisting of 200-nm gold on 200-nm palladium is used. Palladium serves as both an adhesion layer and a diffusion barrier. Attempts were made to use thinner structures with 150-nm of each metal but the film strength was not satisfactory. A minimum thickness of 200 nanometer for each metal is required to ensure the success of wire bonding. Both metal films were deposited using a CHA e-beam evaporator and standard evaporation recipes provided by the Center for Nano and Micro Manufacturing (CNM2).

- For the n-side contact, a 1-nanometer alumina tunneling layer was deposited using atomic layer deposition (ALD) before a 70-nanometer nickel layer was evaporated on

top. The alumina layer served as a tunneling layer to separate the nickel from the germanium surface. This reduces the barrier induced by Fermi-level pinning and forms a contact closer to the ideal Ohmic behavior. The ALD deposition was performed using a Picosun R-200 plasma-enhanced ALD (PE-ALD) with CNM2 standard alumina recipe (TEMAH and H_2O). The nickel layer was evaporated using the same e-beam evaporator as used for the p-side metalization.

Figure 10. CHA e-beam evaporator

Figure 11. Picosun R-200 plasma-enhanced ALD

Chapter 3

3.1 Device Packaging

The fabricated devices were to be sent to the Advanced Light Source (ALS) to be tested under high-energy X-ray sources. In order to be compatible with the testing setup at ALS, the devices need to be packaged with SubMiniature version A (SMA) coaxial interfaces. The vertical nature of the device requires electrical contact on both the front and the back of the device. X-ray illumination will be impinging on the device from the p-type side so the bonding on p-side must be transparent.

The first few batches of devices were packaged using wire bonding. A West Bond 7700E thermosonic ball bonder was used to create gold ball bonding on the fabricated bonding pads. The p-side of the device was wire bonded to the edge of the gold-plated SMA connector. The n-side of the device was connected to the center SMA conductor using silver epoxy. The epoxy also provided adhesion strength so the device does not fall out.

Due to continued device losses to vibration and physical shock during transportation, later AXUV-clone devices were packaged with silver epoxy on both sides, utilizing the placement of the bonding pads on the p-side. Small droplets of silver epoxy can be deposited on the corner with the bonding pad and make connection with the side wall of the SMA connector without blocking the active region of the device. This bonding technique proved more resilient and stable compared to wire bonding. Figure 12(a) and 12(b) shows the cross-section diagrams of both bonding techniques.

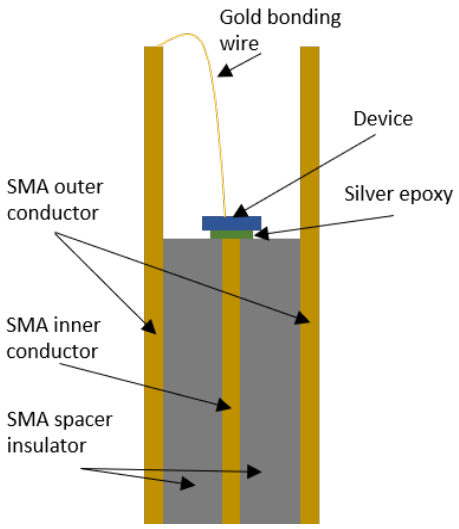

Figure 12(a). Wire-epoxy hybrid bonding diagram.

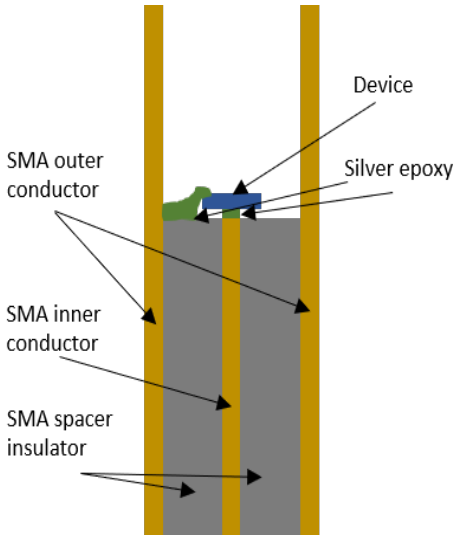

Figure 12(b). Double-side epoxy bonding diagram.

3.2 DC Measurements

3.2.1 Measurement Setup

The DC measurements were taken with unpacked devices using a 2-probe probe station and an HP 4155A semiconductor parameter analyzer. All devices tested were ring diode devices

with 60 μm intrinsic regions. Due to the limits of the parameter analyzer setup in CNM2, the voltage sweep range was limited to (-20 V, 20 V) and the current compliance is 100 mA.

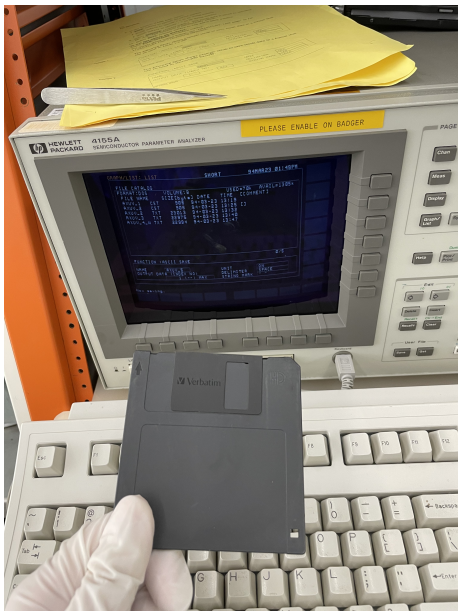

Figure 13. HP 4155A semiconductor parameter analyzer.

Individual devices were placed on the probe station chuck. The chuck provided grounding connection on the n-type side. Ultra-fine Cat Whisker probes from Micromanipulator were mounted onto the probe arms and brought into contact with the bonding pad on the p-type side. Minimal contact pressure was exerted to prevent penetration in the metalization layer. Four I-V response acquisitions were made on each of the 15 testing devices using the aforementioned maximum range and compliance. For all measurements, the lid of the probe station remained open with the microscope illuminator turned off.

The main goal of the DC measurements is the model the switching behavior of fabricated devices to verify the operational status of the p-i-n junction. Irregular or unexpected I-V response may indicate inoperative devices due to fabrication damages or wafer defects. The yield of the fabrication process may also be estimated.

3.2.2 I-V Response

Of the 15 devices measured, two showed unexpected I-V behavior without the switching characteristics of a p-i-n diode. These two devices were considered defective and their data were excluded. For the 13 functional devices, 44 total I-V traces were collected and plotted. All traces with an average I-V profile is shown in Figure 14. The current behavior near +20 V bias is believed to be caused by the semiconductor parameter analyzer as it differs significantly from any known device behavior. Figure 15 shows a semi-log I-V plot of the area of interest (2 V to -20 V).

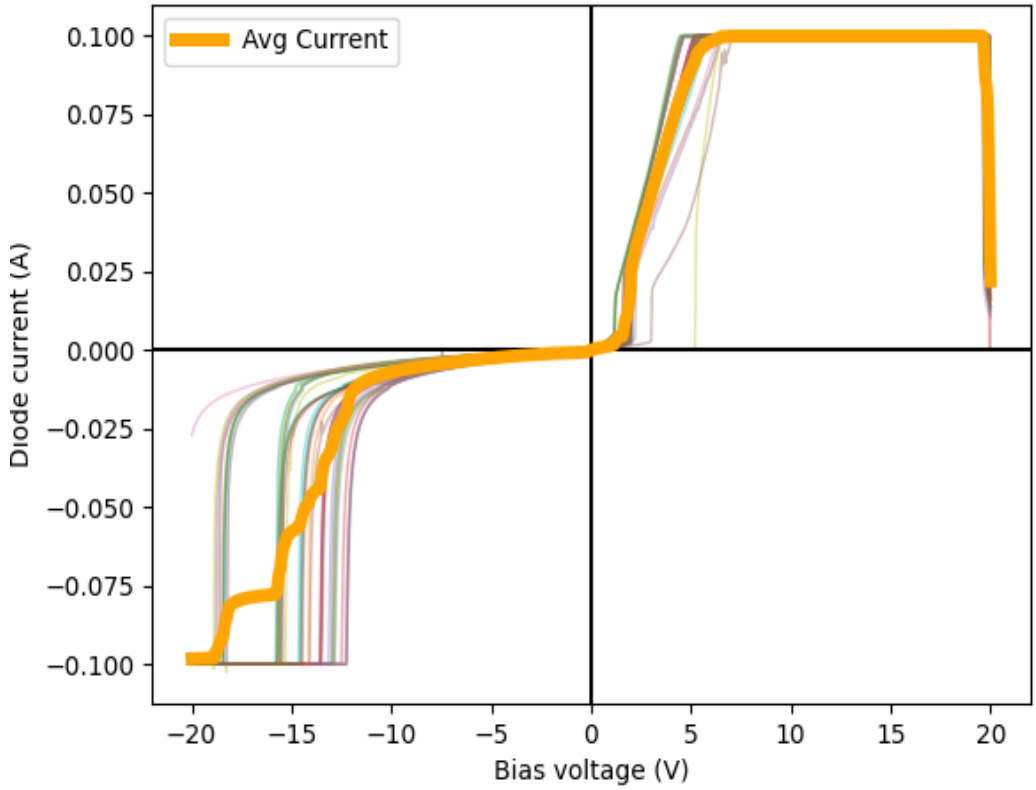

Figure 14. 10 μm ring devices I-V characteristics with average.

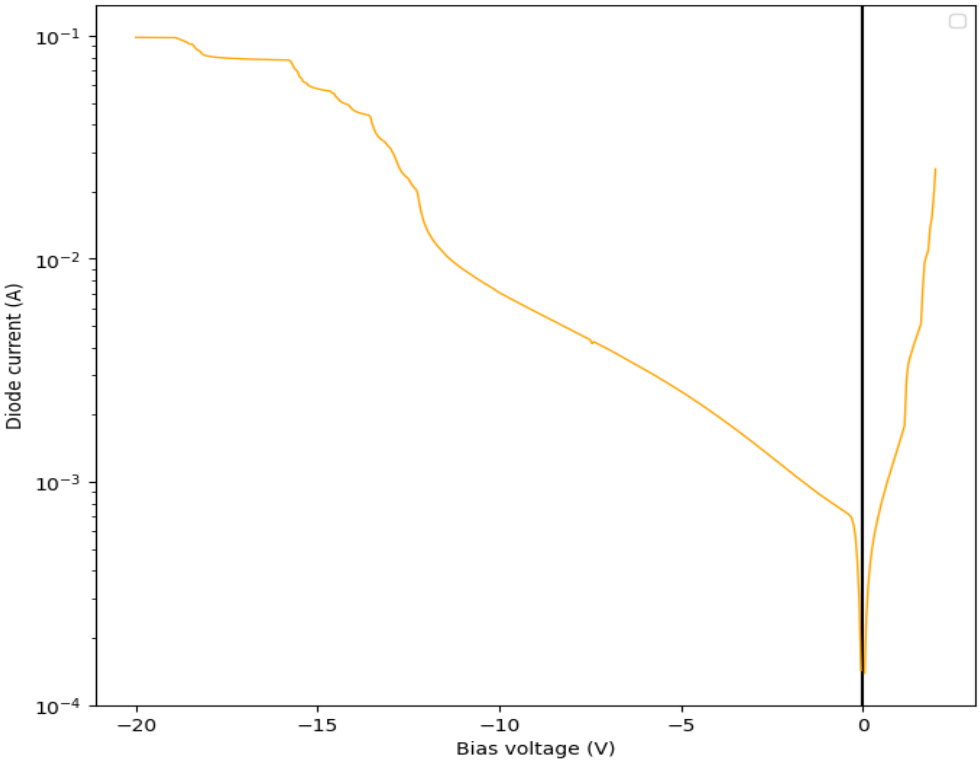

Figure 15. Semi-log I-V characteristics of 10-μm ring devices from 2V to -20 V.

From the obtained I-V traces, it is evident that the fabricated devices exhibit clear switching behavior with an average turn-on voltage of $\sim$ 1.60 V. In the forward bias region, the current scales very linearly with increases in voltage. This indicates that both the p-side and the n-side metallic junctions are highly Ohmic. The same conclusion may be made from the near-vertical reverse breakdown current profiles.

Analyzing the reverse-bias region of the average I-V curve, we see that the average breakdown voltage was -11.85 V, with some devices breaking down at around -20 V. The differences in breakdown voltage from device to device may originate from process variances and localized wafer defects. The average reverse saturation current was 3.9 mA. The continuous increase in reverse saturation current before break down is expected as the p- and n-regions of

the device are thin and the doping concentration are relatively low. Under reverse-bias, the quasi-neutral region width will be greatly compressed by the expanding space-charge region, causing slow increases in reverse current. After the onset of breakdown, see that the I-V slope remains steep for all devices tested. The calculated junction resistance in breakdown is 11.84 Ω.

3.3 Transient Measurements

3.3.1 Measurement Setup

Transient measurements were performed on SMA packaged, AXUV-clone devices on a 532-nanometer wavelength, 10-ns pulse-width green laser with a 3 GHz oscilloscope and a source-measurement unit. The laser probe station was an ablation station designed to remove material thin-films repurposed for exciting our p-i-n photodiodes. Packaged devices were taped onto the side of the chuck with the p-type side of the diode facing the incoming laser beam. A bias-tee was used to enable the application of bias and collection of data with a single SMA-to-BNC cable. Figure 16 shows a diagram of the wiring layout on the test setup. The laser was controlled either manually through a button or could be pulsed continuously. For every device tested, the laser was set to continuous mode and 100 consecutive traces were collected at different biasing levels. The oscilloscope was set to trigger automatically on the rising edge of the signal.

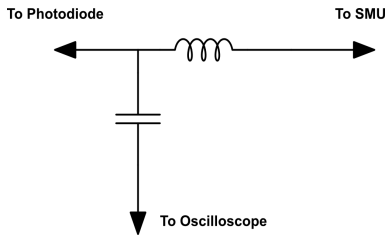

Figure 16. Bias-tee wiring diagram used in AC measurement.

Since the laser setup used was a repurposed ablation station, photon flux, exact pulse-width, and spectrum spread information was not available. The power of the laser was also

controlled with a black-box controller indicating only an arbitrary unit. Our testing will be focused mainly on the rise- and fall-time of the diodes for estimation of frame-rate. It was also in our interest to observe any indication of charging in between consecutive snapshots.

3.3.2 Temporal Response

The 100 traces taken from a germanium p-i-n photodiode with 60 μm intrinsic region thickness were plotted and averaged to show the temporal transient response of the devices when a single 532-nm laser shot lands on the active region, as shown in Figure 17. The device shows a smooth, symmetrical ramp-up and ramp-down behavior as the generated excess carriers are collected at metal contacts. The smooth envelope is expected as most carriers are generated inside the bulk of the intrinsic region close to the center of the device, it takes finite amount of time before these carriers can drift to the p- and n-regions to be detected.

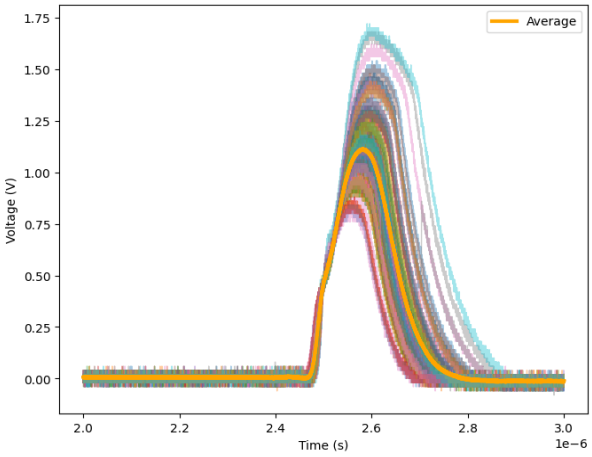

Figure 17. 60-μm AXUV-clone germanium p-i-n diode temporal response at 100 laser power setting and 40 V applied reverse bias.

For comparison, an AXUV silicon-based photodiode was also tested using the same setup under similar conditions. Figure 18 shows the temporal responses of these diodes and an average across 100 snapshots.

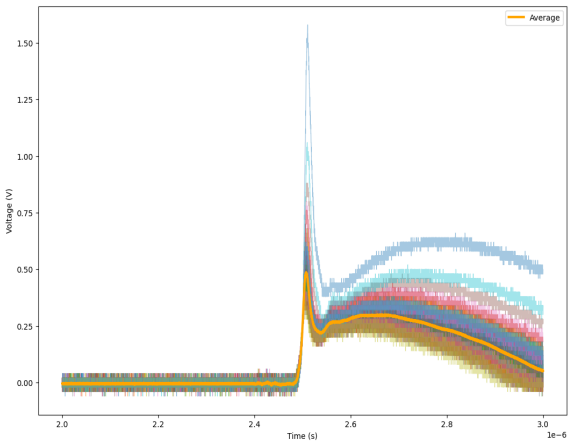

Figure 18. Silicon-based AXUV photodiode temporal response at 100 laser power setting and 48 V applied reverse bias.

By comparing Figure 17 and Figure 18, it is evident that although the silicon AXUV diodes are much faster in rise time compared to our germanium diodes, they have fall times several times longer than our germanium photodiodes at around the same reverse bias. On average, the germanium photodiode rises to 87% of maximum signal strength in 150 nanoseconds while the silicon diodes does so in 20 nanoseconds. However, the germanium photodiodes were capable of discharging and returning from maximum signal strength to 13% maximum signal level in 128 nanoseconds. The silicon reference diode requires an average of 478 ns to drop from maximum signal level to 13%. This gives an average frametime of 278 ns for our germanium photodiodes compared to 528 ns for silicon AXUV diodes.

As designed, the germanium photodiodes provides a much faster discharge time compared to silicon diodes under similar conditions. The drastically faster fall time is more crucial to increasing the speed (bandwidth) of the photodiodes since any residual charge from the

previous frame will distort upcoming frames. The silicon photodiodes does provide faster rise times but rise time in general is not as crucial in imaging as reaching maximum signal strength is not required to generate satisfactory frames. From the same graph we also observe that the maximum average signal strength of germanium photodiodes was 1.11 V at 100 laser power while that of silicon photodiodes was 0.49 V. Our germanium photodiodes were capable of generating signal strength under comparable reverse bias and identical incident laser power 229% of that generated by baseline silicon diodes. This is expected as germanium's higher atomic weight translates into superior stopping power compared to silicon. A higher signal level indicates higher signal-to-noise ratio (SNR) even under low photon flux conditions.

Calculating from the collected data, the germanium photodiode has an SNR of

$$\mathrm{SNR}_{\mathrm{dB}} = 20 \log_{10} \left(\frac{V_{\mathrm{signal}}}{V_{\mathrm{noise}}} \right) = 20.9$$

at 40 V of reverse bias and 100 laser power setting. In our case, the SNR is considered to be limited by the amount of illumination power provided by the laser setup. The laser spot size was considerably small ($\ll$10%) compared to the active region area of the device. Due to the open-sided nature of the testbench, we were also unable to completely shield the device from ambient light sources. Signal generation from ambient light may be contributing to the noise floor of the photodiode. The potential SNR of the device operating in dark environments with higher reverse bias (as designed) and 100% illumination coverage of the active region should be much higher.

Chapter 4

4.1 Conclusion

In this research, a wafer-to-device fabrication process was developed for a novel germanium p-i-n photodiode design utilizing epitaxially-grown pre-doped germanium wafers. Significant work was done to adapt common silicon-oriented process steps and recipes to be suitable for application on germanium. Photoresist processing recipes were developed empirically to reliably produce consistent, high-quality photoresist thin-films. A surface passivation technique utilizing polyimide films was implemented for reduced surface states and decreased dark currents. Active efforts were made to achieve near-perfect Ohmic behavior on both n-type and p-type metallic junctions in both forward- and reverse-biased situations. The fabrication process was refined and optimized to achieve a 86.7% yield and a 2-day lead time.

Fabricated ring diodes with 10-μm intrinsic absorption regions were tested for large-signal (DC) behavior with a -20 V to 20 V voltage sweep. The I-V behavior showed clear switching behavior with a average breakdown voltage of -11.85 V under ambient illumination. The maximum observed breakdown voltage was above -20 V. The average reverse-bias saturation current was 3.9 mA under ambient illumination. Major contributors to the higher-than-usual reverse saturation current include defects from dicing, shrinking of quasi-neutral regions under reverse bias, and generation from ambient illumination. In the reverse-bias breakdown region, the observed resistance was 11.84 Ω. Forward-biased regions also showed clear, steady Ohmic behavior. This confirmed the effectiveness of the metalization structures implemented for reduced Fermi-level pinning on the n-type side.

Devices made to mimic commercial AXUV silicon-based photodiodes were fabricated using the same process and tested for AC (temporal) responses using a 532-nm, 10-ns laser. A reference silicon AXUV diode was also tested under similar conditions to provide comparison. Transient testing showed that our germanium photodiodes achieved an average rise time to

87% maximum signal level of 150 ns and an average fall time to 13% maximum signal level of 128 ns. Compared to the 20 ns rise time and 478 ns fall time recorded from the AXUV diode, we have strong evidence that, under comparable conditions, our germanium p-i-n photodiodes could achieve a frametime 1.9 times faster than silicon photodiodes. Transient measurements also showed that, with comparable reverse applied bias and total incident power, our germanium photodiodes could generate signals 229% of that generated by silicon diodes of the same specifications. Both data strongly suggest that our germanium p-i-n photodiodes are superior at photon direct-imaging than existing silicon equivalents. The measured average signal-to-noise ratio of our germanium photodiodes was 20.9 dB with ambient illumination, low reverse-bias, and partial laser coverage. It is expected that the maximum available dynamic range and SNR will be much higher under actual operating conditions.

The purpose of the fabricated germanium p-i-n photodiodes is direct imaging of high-energy photons in the hard X-ray range above 20 keV. Imaging at these energy ranges proves to be hard due to the relatively weak absorption of hard X-ray photons in most semiconductor materials. With satisfactory electrical properties, germanium provides superior stopping power in the hard X-ray range. Based on the data collected from these prototype devices, we are very confident that the final device will provide high quantum-efficiency, high spatial resolution, and fast temporal response when deployed for direct hard X-ray imaging in various diagnosis settings. The wafer-to-device fabrication process developed for prototyping will also provide solid foundation for the mass-production of final devices.

4.2 Future Works

As a proof-of-concept, this research only focused on small-scale fabrication and measurement of prototype germanium photodiodes. Many aspects of this research could be improved, expanded, or further explored to enhance the efficiency of the fabrication process or improve the performance of fabricated devices. We have identified and listed here three major points

for possible improvements.

4.2.1 Wafer Handling

In order to support rapid prototyping and minimize material loss, our fabrication process were performed using 30x30 mm germanium chips diced from 6-inch wafers. The reduced sample size also reduced production throughput and required the use of custom tools to handle the samples. Germanium is a fragile material that would shatter when exposed to external shock or deformed by even minimal amounts. With sufficient custom tooling, it is possible to provide support for 6-inch wafers in all processing steps to reduce fracture chances and achieve production using complete 6-inch wafers. The use of whole wafers reduces time spent repeating certain processing steps and can be better automated or optimized. In steps such as oxide stripping and photoresist development, it is preferred to reduce the amount of time individual samples spent waiting for other samples to complete. Developing and achieving wafer-level production will likely improve both production throughput, production yield, and device performance.

4.2.2 Surface Cleaning and Passivation

Much like silicon, germanium oxidizes when brought in contact with oxygen present in the atmosphere. Unlike silicon, however, germanium does not form a uniform, dense oxide film that naturally passivates the surface. Instead, germanium has multiple oxidation states with multiple radical oxides. The native oxide film on germanium introduces surface traps that promote dark current generation. Native oxide layers will also impede metalization. In this research, a single-step HCl etch was used to remove native oxide films before the surface is passivated permanently with polyimide. The brief exposure to atmosphere between the wet chemical etch and passivation can still leave a thin layer of native oxide. If the oxide removal process can be integrated into the permanent passivation process, or if the sample can be kept from oxygen exposure during handling between the cleaning and passivation

steps, the device surface cleanliness can be improved. This will lead to reduced dark current and improved metal contact performance.

4.2.3 Photodiode Arrays

As a proof-of-concept device, our photodiodes only have one pixel per package. This is sufficient for developing fabrication processes and evaluating device designs. However, for our germanium photodiodes to be useful in real-world settings, it must be able to be scaled up to arrays of meaningful size for image acquisition. In order to expand the knowledge learned from our prototype and expand the technology, extensive testing such as cross-talk testing must be conducted. Our packaging technique may not apply to array devices as well due to the limited bonding area in arrays.

Appendix A

The following process is for fabrication of AXUV-clone germanium photodiodes. Many process parameters were determined empirically and must be verified again for different samples/devices.

1.1 Sample Cleaning

1. Submerge samples into acetone.
2. Let sample remain in sonicator for 5 minutes.
3. Remove samples from acetone and submerge into methanol.
4. Let sample remain in sonicator for 5 minutes.
5. Remove samples from methanol and submerge into IPA.
6. Let samples remain in sonicator for 5 minutes.
7. Rinse samples under DI water for 30 seconds.
8. Blow dry samples with N_2.

1.2 Photoresist Application

1. Turn on hot plate and set temperature to 200 °C. Wait for the temperature to settle.
2. Place samples on hot plate and bake for 7 minutes.
3. Remove samples from the hot plate and place on a borosilicate glass panel to cool down.
4. Set hot plate to 120 °. Place borosilicate glass panel on hot plate to be heated together. Wait for the temperature to settle.

5. Load samples into spinner. Choose the appropriate chuck for the sample size and center the samples on the spindle.

6. Open the photoresist bottle. Pour NR78-8000P onto the sample surfaces from a height of $\sim$1 cm. Photoresist should cover $\sim$ 50% of the sample surfaces.

7. Remove any visible air bubble from the resist blob using the tip of a pipette.

8. Spin the samples at 1750 RPM for 40 seconds. Ramp up to 1750 RPM at a rate of 1750 RPM/s.

9. Transfer samples from the spinner to the heated borosilicate glass panel. Bake the sample for 5 minutes.

10. Place samples in appropriate containers and wrap with aluminum foil to prevent accidental exposure.

1.3 Exposure and Development 1

Alignment and exposure dosage tests must be conducted before actual fabrication.

1. Load the AXUV reticle into the optical column of the stepper.

2. Choose the correct spacer for sample chuck based on alignment test results.

3. Load samples into the stepper optical stage.

4. Expose quadrant 2 of the mask with the correct dosage.

5. Remove samples from the stepper.

6. Set hot plate to 110 °. Wait for the temperature to settle.

7. Put the samples onto the hot plate. Bake for 5 minutes.

8. Remove the samples from the hot plate and wait for them to cool.

9. Submerge samples into RD-6. Lightly agitate the bath for 35 s.

10. Remove the samples from the RD-6 and immediately rinse under running DI-water for 30 s.

11. Dry the samples with N_2 gas.

12. Check the exposed patterns under an optical microscope.

1.4 Isolation Etching

1. Clean the surface of a sapphire carrier wafer with IPA rinse. Rinse with DI water and dry with N_2.

2. Apply vacuum oil on the surface of the sapphire carrier. Gently place the samples on the vacuum oil layer and apply moderate pressure to secure them. Make sure the p-type side is facing up.

3. Load the sapphire carrier into the RIE chamber.

4. Set the chamber parameters of the RIE machine to be 150 W plasma power, 40 sccm CF_4, 5 sccm O_2. Set etch time to be 5 minutes.

5. Execute the RIE recipe and wait for completion.

6. Remove sapphire carrier from the RIE chamber.

7. Gently push samples off the edge the sapphire carrier.

8. Clean both the samples and the sapphire carrier as shown in Sample Cleaning.

1.5 Photoresist Removal

1. Heat RR-41 to 85 °C on hot plate.

2. Submerge samples into hot RR-41. Wait for 5 minutes.

3. Check if all photoresist layer has dissolved/detached by rinsing the samples with DI water Look for specks of PR still attached to the sample surface and cause streaks in the water flow. Take out samples with all PR removed.

4. Clean the samples as in Sample Cleaning.

1.6 Polyimide Application

1. In a large beaker, mix 36% HCl : DI water with ratio 1:4.

2. Submerge samples in diluted HCl for 1 minute.

3. Take samples out and rinse with running DI water for 20 seconds.

4. Dry samples with N_2.

5. Immediately submerge samples in VM-652 adhesion promoter for 10 seconds.

6. Dry samples with N_2.

7. Turn on two hot plates. Set to 90 °C and 150 °C.

8. Place samples into the spinner. Choose the appropriate chuck and center the sample.

9. Apply PI-2610 uniformly to the center of the samples using a syringe. PI-2610 should cover $\sim$ 30% of samples surface. Remove any visible air bubble with the tip of a pipette.

10. Spin the samples at 500 RPM for 5 seconds and then at 4000 RPM for 30 seconds. The ramp up time between spins should be 5 seconds.

11. Unload the samples and transfer to the hot plate. Bake for 3 minutes at 90 °C and 3 minutes at 150 °C.

12. Transfer samples to oven. Set oven target temperature to 350 °C with ramp rate 4 °C/min. Hold at 350 °C for 30 minutes. Allow the samples to return to room temperature naturally before opening the oven.

1.7 Exposure and Development 2

1. Apply photoresist as in Photoresist Application
2. Prepare the stepper and samples as in Exposure and Development 1.
3. Expose with the same exposure dosage and quadrant 3.
4. Develop pattern as in Exposure and Development 1.

1.8 Polyimide Etch

1. Prepare samples and sapphire carrier wafer as in Isolation Etch.
2. Set RIE chamber parameter to 204 W plasma power, 7 sccm O_2 flow, 192 mTorr chamber pressure. Set etch time to 15 minutes.
3. Unload and clean the samples and carrier wafer as in Isolation Etch.

1.9 Alumina ALD

1. Clean the patterned ALD carrier Si wafer in IPA and rinse with DI water. Dry with N_2.
2. Place samples into appropriate pockets on the carrier wafer with n-type side facing up.
3. Load carrier wafer into ALD load lock.
4. Select TMA-H_2O ALD recipe. Pulse for 10 cycles for 1 nm deposition thickness.
5. Wait for the ALD process to finish automatically. Unload the samples.

1.10 Exposure and Development 3

1. Apply photoresist as in Photoresist Application
2. Prepare the stepper and samples as in Exposure and Development 1.
3. Expose with the same exposure dosage and quadrant 4.
4. Develop pattern as in Exposure and Development 1.

1.11 E-beam Evaporation

1. Clean the bare metalization carrier Si wafer in IPA and rinse with DI water. Dry with N_2.
2. Using polyimide tape, carefully secure the samples to the carrier wafer with the side to be deposited facing up. Ni should be deposited on the n-type side. Au and Pd should be deposited on the p-type side.
3. Follow the E-beam evaporator SOP and load samples into the machine with all crucibles needed.
4. Nickel deposition thickness should be 70 nm. Gold deposition thickness should be 200 nm followed by a palladium deposition of 200 nm. The samples need to be unloaded and flipped around between n-type and p-type side deposition.
5. When done, carefully unload the samples from the carrier wafer.

1.12 Liftoff

1. Heat RR-41 to 85 °C on hot plate.
2. Submerge samples into hot RR-41.

3. Check every 10 minutes if all photoresist layer has dissolved/detached by rinsing the samples with DI water Look for specks of PR still attached to the sample surface and cause streaks in the water flow. Take out samples with all PR removed.

4. Gently rinse with DI water. Dry with N_2.

References

[1] J. E. Wickersham, H.-S. Park, P. M. Bell, J. A. Koch, O. L. Landen, and J. D. Moody, "Imaging detectors for 20–100 kev x-ray backlighters in high-energy-density experimental science petawatt experiments," *Rev. Sci. Instrum.*, vol. 75, no. 10, pp. 4051–4053, Oct. 2004.

[2] *AXUV Series Absolute UV Silicon Photodiodes*, Opto Diode Corp., 2020. [Online]. Available: https://www.aptechnologies.co.uk/images/Data/ODC/AXUV-SeriesDataBook_05Aug20.pdf

[3] L. M. P. Fernandes, F. D. Amaro, A. Antognini, J. M. R. Cardoso, C. A. N. Conde, O. Huot, P. E. Knowles, F. Kottmann, J. A. M. Lopes, L. Ludhova, C. M. B. Monteiro, F. Mulhauser, R. Pohl, J. M. F. dos Santos, L. A. Schaller, D. Taqqu, and J. F. C. Veloso, "Characterization of large area avalanche photodiodes in x-ray and VUV-light detection," *J. Instrum.*, vol. 2, no. 08, p. P08005, Aug. 2007.

[4] G. Lioliou and A. M. Barnett, "Gallium arsenide detectors for x-ray and electron (beta particle) spectroscopy," *Nucl. Instrum. Methods Phys. Res. A*, vol. 836, pp. 37–45, Nov. 2016.

[5] S. Seltzer, "Tables of x-ray mass attenuation coefficients and mass energy-absorption coefficients, NIST standard reference database 126," 1995.

[6] G. Lucovsky, M. E. Lasser, and R. B. Emmons, "Coherent light detection in solid-state photodiodes," *Proc. IEEE*, vol. 51, no. 1, pp. 166–172, Jan. 1963.

[7] M. S. Tyagi, *Introduction to semiconductor materials and devices.* John Wiley & Sons, 2008, pp. 308–310.

[8] E. Gaubas and J. Vanhellemont, "Dependence of carrier lifetime in germanium on resisitivity and carrier injection level," *Appl. Phys. Lett.*, vol. 89, no. 14, p. 142106, Oct. 2006.

[9] S. M. Sze, *Physics of Semiconductor Devices*, 2nd ed. John Wiley & Sons, 1981, pp. 754–760.

[10] W. van Roosbroeck and W. Shockley, "Photon-Radiative recombination of electrons and holes in germanium," *Phys. Rev.*, vol. 94, no. 6, pp. 1558–1560, Jun. 1954.

[11] S. Kalashnikov, "Studies on the recombination of electrons and holes in germanium," *Journal of Physics and Chemistry of Solids*, vol. 8, pp. 52–59, 1959. [Online]. Available: https://www.sciencedirect.com/science/article/pii/0022369759902732

[12] K. P. T. S. G. Kalashnikov, "Volume recombination in al-doped ge," *Zhurnal Tekhnicheskoic Fiziki*, 1958.

[13] H. Yoon, K. Edmondson, G. Kinsey, R. King, P. Hebert, R. Ahrenkiel, B. Cavicchi, and N. Karam, "Minority carrier lifetime and radiation damage coefficients of germanium," in *Conference Record of the Thirty-first IEEE Photovoltaic Specialists Conference, 2005.*, 2005, pp. 842–845.

[14] A. Kumar, "Ohmic contacts to homoepitaxially grown p-type and n-type germanium," Master's thesis, ProQuest Dissertations Publishing, 2020. [Online]. Available: https://www.proquest.com/docview/2442402144

[15] *RCA WAFER CLEAN SOP*, University of Louisville Micro/Nano Technology Center, April 2020. [Online]. Available: https://louisville.edu/micronano/files/documents/standard-operating-procedures/RCAclean_SOP.pdf

[16] T. Kawase, A. Mura, K. Dei, K. Nishitani, K. Kawai, J. Uchikoshi, M. Morita, and K. Arima, "Metal-assisted chemical etching of ge(100) surfaces in water toward nanoscale patterning," *Nanoscale Research Letters*, vol. 8, no. 1, 2013.

[17] *NEGATIVE RESIST NR78-8000P*, Futurrex Productivity Tools. [Online]. Available: https://ucdavis.app.box.com/s/6wqorcuq46bmzypjajn5ox2zsd6zdzy4

[18] A. Campo, C. Cardinaud, and G. Turban, "Investigation of si and ge etching mechanisms in radiofrequency cf2-o2 plasma based on surface reactivities," *Plasma Sources Science and Technology*, vol. 4, no. 3, p. 398, aug 1995. [Online]. Available: https://dx.doi.org/10.1088/0963-0252/4/3/009

[19] J. Kim, J. McVittie, K. Saraswat, Y. Nishi, S. Liu, and S. Tan, "Germanium surface cleaning with hydrochloric acid," *ECS Transactions*, vol. 3, no. 7, p. 1191–1196, 2006.